NANOSYSTEMS:
PHYSICS, CHEMISTRY, MATHEMATICS

Original article

Iyakhmaeva A.A., et al. *Nanosystems: Phys. Chem. Math.*, 2025, **16** (6), 837–849.
http://nanojournal.ifmo.ru
DOI 10.17586/2220-8054-2025-16-6-837-849

Formation of 2:1 Li–Fe-phyllosilicate with montmorillonite-like structure in hydrothermal conditions

Asiyat A. Iyakhmaeva[1], Ekaterina K. Khrapova[1], Lev A. Lebedev[1], Nadezhda V. Glebova[1], Valentin G. Semenov[2], Andrey V. Kopylov[3], Andrei A. Krasilin[1]

[1]Ioffe Institute, St. Petersburg, Russia

[2]Institute of Chemistry, St. Petersburg State University, St. Petersburg, Russia

[3]RITVERC JSC, St. Petersburg, Russia

Corresponding author: Andrei A. Krasilin, ikrasilin@mail.ioffe.ru

PACS 81.20.-n, 82.80.Ej

ABSTRACT We report on hydrothermal synthesis and structural characterization of Li–Fe-montmorillonite (MMT). To date, this 2:1 type phyllosilicate attracts attention due to such properties as high ion mobility, hydrophilicity, electrical and thermal resistance. Due to that, various MMTs may serve as perspective components of Li-ion batteries (electrolyte and separator fillers, as well as protective buffer layer on top of Li metal anode). Scarce data on synthetic Li–Fe^{3+}-MMTs motivated us to investigate formation process and structure features of such phyllosilicate by X-ray diffraction, UV-visible and Mössbauer spectroscopy, and other methods. We established critical Fe^{3+} content and temperature range needed for almost single-phase MMTs formation. Around 20 % of total Fe may occupy tetrahedral site of MMT layer. Thermal behavior of Li–Fe-MMT strongly depends on hydrothermal synthesis conditions because of different Li^+ amount present in the interlayer space and in the layer vacancies.

KEYWORDS phyllosilicate, hydrothermal synthesis, isomorphism, X-ray diffraction, Mössbauer spectroscopy

ACKNOWLEDGEMENTS This work was supported by the St. Petersburg Science Foundation and the Russian Science Foundation [grant number 25-19-20096], https://rscf.ru/project/25-19-20096/.

FOR CITATION Iyakhmaeva A.A., Khrapova E.K., Lebedev L.A., Glebova N.V., Semenov V.G., Kopylov A.V., Krasilin A.A. Formation of 2:1 Li–Fe-phyllosilicate with montmorillonite-like structure in hydrothermal conditions. *Nanosystems: Phys. Chem. Math.*, 2025, **16** (6), 837–849.

1. Introduction

Among the wide variety of layered silicates, the so-called 1:1 and 2:1 phyllosilicates are distinguished. Some 1:1 phyllosilicates, due to their asymmetric layer structure, in which there is one tetrahedral sheet for every octahedral sheet, are capable of spontaneously scrolling into nanotubes and nanoscrolls [1–4]. As for the 2:1 phyllosilicates, this possibility is vanished by the conjunction of two tetrahedral sheets and one octahedral sheet between them [5–7]. Despite the disappearance of asymmetry, such phyllosilicates exhibit other remarkable properties, such as, for example, in the case of $(Ca,Na)_y(Mg,Fe)_2[(Al,Si)_4O_{10}](OH)_2$ layers with montmorillonite (MMT) structure – the possibility of intercalation of various cations into the interlayer space in order to compensate for the excess negative charge of the layer. This feature has led to the widespread use of natural and synthetic MMTs as ion-exchange adsorbents [8–11].

In addition to environmentally hazardous pollutants, the labile interlayer space of MMT is modified by functional substances of organic nature [12–14], as well as by catalytically active phases and their precursors [15–17].

Another noteworthy practical application of MMT is related to energy storage devices, including lithium-ion batteries [18, 19]. The combination of the dielectric nature of the MMT layer [20], high thermal stability [21], mechanical properties [22, 23], hydrophilicity due to OH groups and high cation mobility in the interlayer space makes these phyllosilicates promising components of separator membranes and semi-solid electrolytes. Thus, a functional coating of a polypropylene separator based on MMT and polyvinyl alcohol as a binder was proposed in [24]. Lithium ion transport was achieved more uniformly through the regularized interlayer space of MMT than through the separator's pore system. A more uniform ion flow led to a more uniform distribution of ions across the anode surface and to a minimization of dendrite formation processes. A similar ability to block the growth of dendrites and the associated longer operation of the battery model with a MMT-based membrane was also noted in [25, 26]. The effect of increasing the ionic conductivity and electrochemical stability of semi-solid electrolytes by introducing MMT phases was noted in [27–29].

Here, we investigate the formation processes of $Li_{2x}Fe_{2-2x}Mg_{2x}Si_4O_{10}(OH)_2$ phyllosilicate under hydrothermal conditions immediately after the precipitation in excess of LiOH. A number of studies have been devoted to the creation of Li-containing MMT via ion exchange in the mineral [30–32], while information on the synthesis of these compounds

by hydrothermal methods is less common. The use of Fe^{3+} cations instead of Al^{3+}, which are more traditional for MMT, opens up additional possibilities for changing the charge state ($Fe^{2+/3+}$), the appearance of a magnetic response, and monitoring the state of iron using Mössbauer spectroscopy [33]. A separate issue was the assessment of the maximum Fe^{3+} content in the phyllosilicate layer, as well as the possibility of substituting Si^{4+} in the tetrahedral position in analogy with Al^{3+}.

2. Materials and methods

2.1. Phyllosilicate synthesis

The synthesis of $Li_{2x}Fe_{2-2x}Mg_{2x}Si_4O_{10}(OH)_2$ (x = 0.5, 0.6, 0.7, 0.8, 0.9, 1) phyllosilicate consisted of two main stages: reverse coprecipitation and subsequent hydrothermal treatment of the resulting suspension. The following reagents were used during the synthesis: amorphous SiO_2 (Aerosil A-300), $LiOH{\times}H_2O$, $MgCl_2{\times}6H_2O$, $FeCl_3{\times}6H_2O$. All reagents were purchased from "Vekton", Russia. In the first stage, a sample of about 3 g SiO_2 was mixed with a 2.7 – 3.2 g (depending on x) $LiOH{\times}H_2O$ and 400 ml of distilled water for 30 minutes using magnetic stirrer. In a separate beaker filled with 200 ml of distilled water, iron and magnesium chlorides were dissolved, taken in the ratio required by the desired formula. Next, using a peristaltic pump, the chloride solution was added dropwise aerosil and alkali under intensive stirring. The feed rate was approximately 1 – 2 drops of solution per second.

The resulting suspensions were subjected to hydrothermal treatment for 7 days in autoclaves with 20 ml PTFE liners at temperatures of 200 °C and 240 °C. Additionally, a sample with x = 0.5 was treated at 350 °C for 9 hours in a 400 ml Ti-lined stainless steel autoclave. The resulting samples were washed twice with distilled water by centrifugation and air-dried at 80 °C. The dried phyllosilicates were ground with an agate mortar.

2.2. Powder X-ray diffraction

Powder X-ray diffraction (PXRD) analysis was performed using a DRON-8N powder X-ray diffractometer (Burevestnik, Russia) with a copper anode ($\lambda = 1.54186$ Å) and a Ni K_β filter. The diffractometer was equipped with a Mythen 2R 1D linear detector (DECTRIS Ltd, Switzerland). Measurements were carried out in the Bragg–Brentano geometry in the 2 – 80° 2θ range with a step of 0.01° and an exposure time of 10 s. The sample rotation during the exposure was 0.5 rps. Phase identification was carried out using the open COD database [34] and the PDF-2 database in case of insufficient information from an open source.

The unit cell parameters were calculated using the Rigaku SmartLab Studio II software package using a full-profile method similar to Le Bail (without refinement of atomic coordinates). The phyllosilicate layers were assumed to be predominantly oriented along [001] direction. Crystallite sizes, ignoring possible microstresses, were determined using the Scherrer formula for the [001] direction in order estimate average thickness of phyllosilicate particles. Furthermore, the full-profile analysis was performed using the anisotropic crystallite approximation, that yielded crystallite size averaged over all directions.

2.3. N_2 adsorption and thermal analysis

Low-temperature nitrogen adsorption was carried out using an ASAP 2020 analyzer (Micromeritics, USA). The samples were preliminarily degassed at a temperature of 110 °C to remove adsorbed water until there was no mass change observed. The analysis was carried out in the 10^{-5} – 0.995 relative pressure (P/P_0) range. To calculate the specific surface area, the Brunauer–Emmett–Teller (BET) model [35] was used in the 0.05 – 0.16 P/P_0 range. The total pore volume was calculated at the maximum relative pressure $P/P_0 = 0.995$. For a more accurate analysis of the pore size distribution, the density functional theory (DFT) calculation method was used according to the N_2 on Carbon at 77 K model [36] with slit pores.

Thermal analysis was carried on a Mettler–Toledo TGA/DSC 1 derivatograph with STARe System software (Switzerland) using air blown through the derivatograph chamber at a flow rate of 30 cm^3/min in a uniform temperature increase mode at a rate of 10 °C/min in the temperature range of 35 – 1000 °C. During the heating process, mass (thermogravimetric, TG) and thermal (differential thermal, DTG) curves were recorded.

2.4. Spectroscopic methods

Diffuse reflectance spectra were recorded using an AvaSpec-ULS4096CL-EVO high-resolution spectrometer (Avantes, Netherlands), an AvaSphere-30 integrating sphere, and an AvaLight-XE pulsed xenon source. The resulting diffuse reflectance spectra (R) were processed using the Kubelka–Munk function (1):

$$F(R) = \frac{(1-R)^2}{2R}. \quad (1)$$

The band gap was estimated using the Tauc plot method [37] for both direct and indirect transitions.

Mössbauer spectroscopy was used to obtain information on the qualitative and quantitative distribution of iron ions across various phases and crystallographic sites. Mössbauer spectra of ^{57}Fe were obtained using a Wissel Mössbauer spectrometer (Germany) in constant acceleration mode at room temperature. $6{\times}10^8$ Bq ^{57}Co in a rhodium matrix (Ritverc

GmbH, St. Petersburg, Russia) was used as a gamma source. Velocity scale calibration and isomer shift were determined relative to α-Fe. Spectra processing was performed using MossFit Ver. 3.7 software.

The elemental composition of the samples was determined using a FEI Quanta 200 (USA) scanning electron microscope (SEM), equipped with an EDAX energy-dispersive spectrometer.

3. Results and discussion

3.1. Iron content impact on lattice volume, crystallite size, and textural properties

As a result of hydrothermal treatment at 200 °C, according to PXRD data (Fig. 1a), mainly single-phase samples were obtained. The position of the X-ray diffraction maxima, as well as the ratio of their intensities, indicated the formation of phyllosilicate with a montmorillonite structure with a monoclinic $C2/m$ (12) space group (comparison was made with the Li-containing analogue COD ID 9010956 [38]). Increasing the processing temperature to 240 °C resulted in the observation of significant diffraction maxima belonging to Fe_3O_4 or a solid solution based on it of the type $Mg_yFe_{2-y}O_4$ (COD ID 9003582 [39]) in the case of $x \leq 0.6$. A further increase in the processing temperature led to a more complex phase composition of the sample with $x = 0.5$ due to the formation of α-Fe_2O_3 (COD ID 2101167 [40]) or, similarly, a solid solution based on it. It should be noted that the formation of iron oxides as impurity phases was also observed in the synthesis of 1:1 phyllosilicates with a related crystal structure [41–43]. The difficulties in replacing Mg^{2+} and Si^{4+} with Fe^{3+} lie in the difference in the formal charges of the cations, which complicated the available isomorphism schemes (from the point of view of the need for charge compensation), and in the strong difference in the effective ionic radii [44], especially between Fe^{3+} and Si^{4+}.

The introduction of iron ions into the crystal structure led to an increase in virtually all unit cell parameters (Fig. 1b-e), although these trends were barely visible due to comparatively low crystallinity of the samples and the associated variability of the full-profile analysis procedure. Individual sharp changes in the parameters a, b, and β at low x were most likely caused by a violation of the single-phase nature of the system. The observed spread in the parameter c could have been further enhanced, firstly, by the different filling of the interlayer space and, secondly, by the dependence of the interlayer distance on the number of layers, which is common to various compounds with a layered structure. The increase in the unit cell volume with increasing iron content (with decreasing x) repeated the trends observed for individual parameters (Fig. 1f).

It is interesting to look at the process of changing the unit cell volume from the point of view of the effective ionic radii of Mg^{2+} (72 pm), Fe^{3+} (63 pm in the octahedral and 49 pm in tetrahedral position) and Si^{4+} (26 pm) [44]. The observed increase in the unit cell volume due to substitution only in the octahedral sublayer looks counterintuitive, if we do not take into account the increased size of the cavity, compared to the coordination octahedron, which inevitably arises during the transition from the trioctahedral silicate to the dioctahedral one. Substitution with the removal of part of the Li^+ from the interlayer space was also possible, as was assumed in the original chemical formula. This version of substitution, based on the values of the ionic radii, should lead to at least an increase in a and b, while the impact caused to parameter c is less obvious: on the one hand, Li^+ maintains an increased interlayer distance due to its size, while on the other hand, it is present due to the need for charge compensation. Accordingly, the removal of Li^+ could lead either to a decrease in the interlayer distance for steric reasons or to an increase due to electrostatic repulsion forces between adjacent layers. Substitution with Si^{4+} should lead to an increase in cell volume, although the nearly twofold difference in ionic radii limited mixability. Thus, the increase in unit cell volume with increasing Fe^{3+} content seemed justified in terms of the ionic radii of the cations involved in the substitution processes and could indirectly indicate the presence of a more complex Fe^{3+} distribution among crystallographic positions than had been initially assumed in the stoichiometric calculation.

Figure 1(g) shows the results of determining the crystallite sizes separately for the 001 reflection, as well as the values averaged over all directions, obtained as a result of a full-profile analysis in the approximation of anisotropic crystallite shape. The introduction of Fe^{3+} into the system generally contributed to a decrease in the crystallite size of phases with the montmorillonite structure. The change in this trend for the case of hydrothermal treatment at 240 °C and $x < 0.7$ was associated with the release of some of the iron ions into the oxide phase. Compared to the average values, the crystallite sizes along the 001 direction were virtually independent of temperature. An increase in the discrepancy between these two dependences suggests that MMT particles became more anisotropic with increasing treatment temperature and most likely grew in directions perpendicular to 001.

Figure 2 shows nitrogen adsorption/desorption isotherms and pore size distributions obtained from the adsorption branch of the curve. All isotherms can be classified as type IV, with a developed mesoporous structure. A sharp rise at the initial stage indicated the presence of micropores in the samples. Hysteresis loops were of the mixed H2-H3 type, which could be associated with a complex, irregular porous structure. The most likely pore shapes for this type of hysteresis loop were bottle-shaped and slit-shaped. Apparently, slit-shaped pores could be located both in the interlayer space of phyllosilicates and in the interparticle space. The non-uniform pore shape, which led to blockage in narrower areas, could be associated with the non-uniform shape of the particles and their broad size distribution. As expected, the specific surface area and pore volume decreased with increasing hydrothermal treatment temperature, which correlated with the

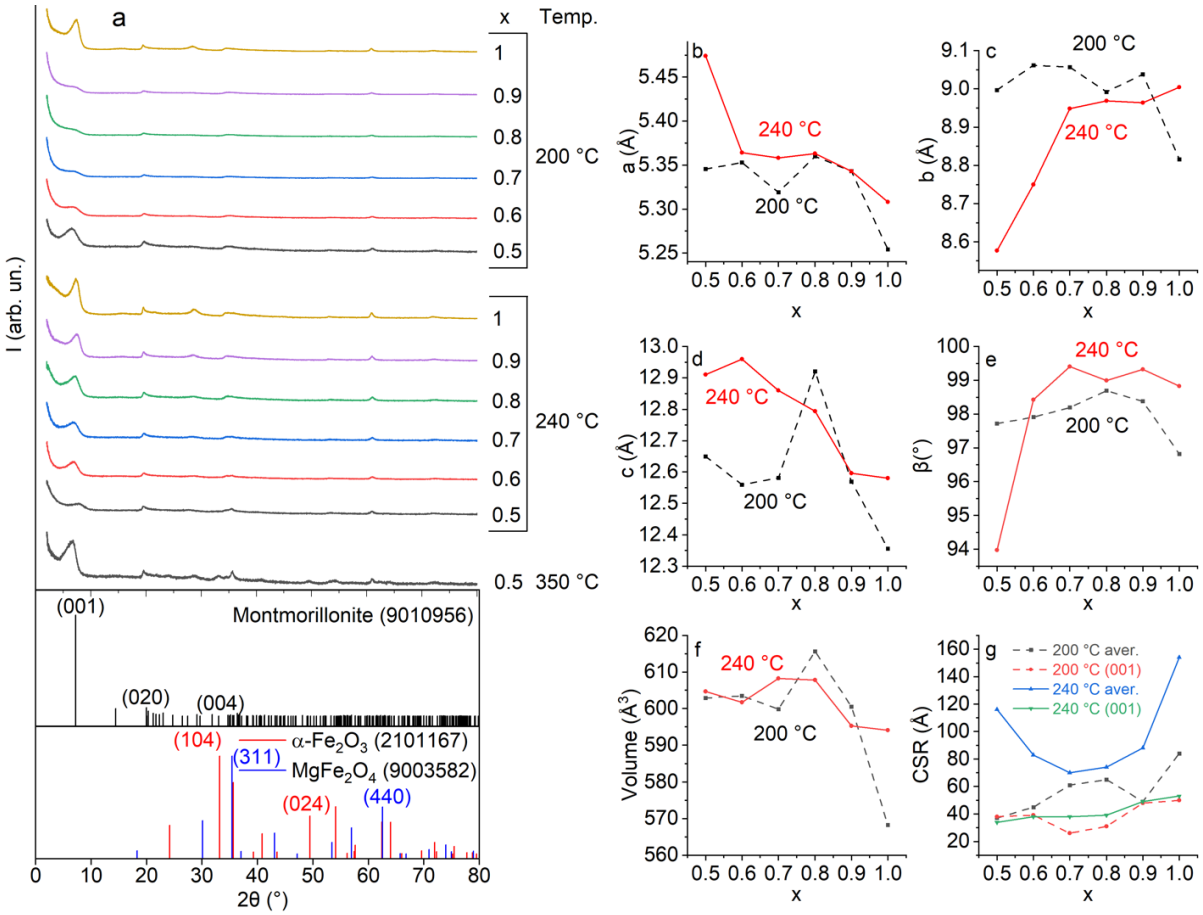

FIG. 1. Results of powder X-ray diffraction analysis. a) PXRD patterns of hydrothermal treatment products together with phase analysis involving COD database. b–f) Calculated unit cell parameters and unit cell volume of MMT phase. g) Crystallite sizes (coherent scattering regions, CSR) of MMT phase

increase in crystallite size as measured by X-ray diffraction (Fig. 1g). The dependence of specific surface area and pore volume on iron content was extreme.

In all cases, the pore size distribution (Fig. 2d–f) showed a maximum in the 1 – 2 nm region, which we believe was due to nitrogen adsorption in the interlayer space of phyllosilicates with a montmorillonite structure. Unfortunately, it was not possible to establish an unambiguous correlation with the interlayer space size according to X-ray diffraction data, which was approximately 50 % of the c parameter, i.e., 0.6 nm (Fig. 1d). The discrepancy between the observed values may be due to both the specific features of the model approximation chosen to describe the adsorption isotherms and the sensitivity of the interlayer distance to the conditions of the adsorption experiment itself (preliminar vacuum and thermal training) [45]. Despite this, the position of the maximum, depending on the hydrothermal treatment temperature, behaved in a manner consistent with the increase in crystallinity, shifting toward smaller sizes due to the compaction of the layer packing (Fig. 2d–f). The distribution in the mesopore region behaved in the opposite direction: with increasing temperature, the center of gravity of the broad maximum shifted from a few to tens of nanometers. This region is formed primarily by interparticle pores, and an increase in particle size typically leads to an increase in the size of the voids between them.

3.2. Element content and iron distribution over phyllosilicate and oxide phases

Table 1 presents the results of EDS analysis of 200 and 240 °C hydrothermal treatment products. In all cases, a deficiency of silicon relative to magnesium and iron cations was observed, which could be caused by both the error of the method itself and the features of the synthesis process. Previously, we noted a systematic deviation of the *Me*:Si ratio from the specified one towards a deficiency of silicon in the case of the formation of impurity oxide phases [46]. A similar situation was observed for the data at high iron contents ($x < 0.7$), especially during hydrothermal treatment at 240 °C. Unfortunately, the lithium content was not available for determination by this method; however, given the observed deficiency of silicon, its underestimated content can also be assumed compared to the calculated chemical formula $Li_{2x}Fe_{2-2x}Mg_{2x}Si_4O_{10}(OH)_2$. The verification experiments that we were able to carry out for x = 0.5 using

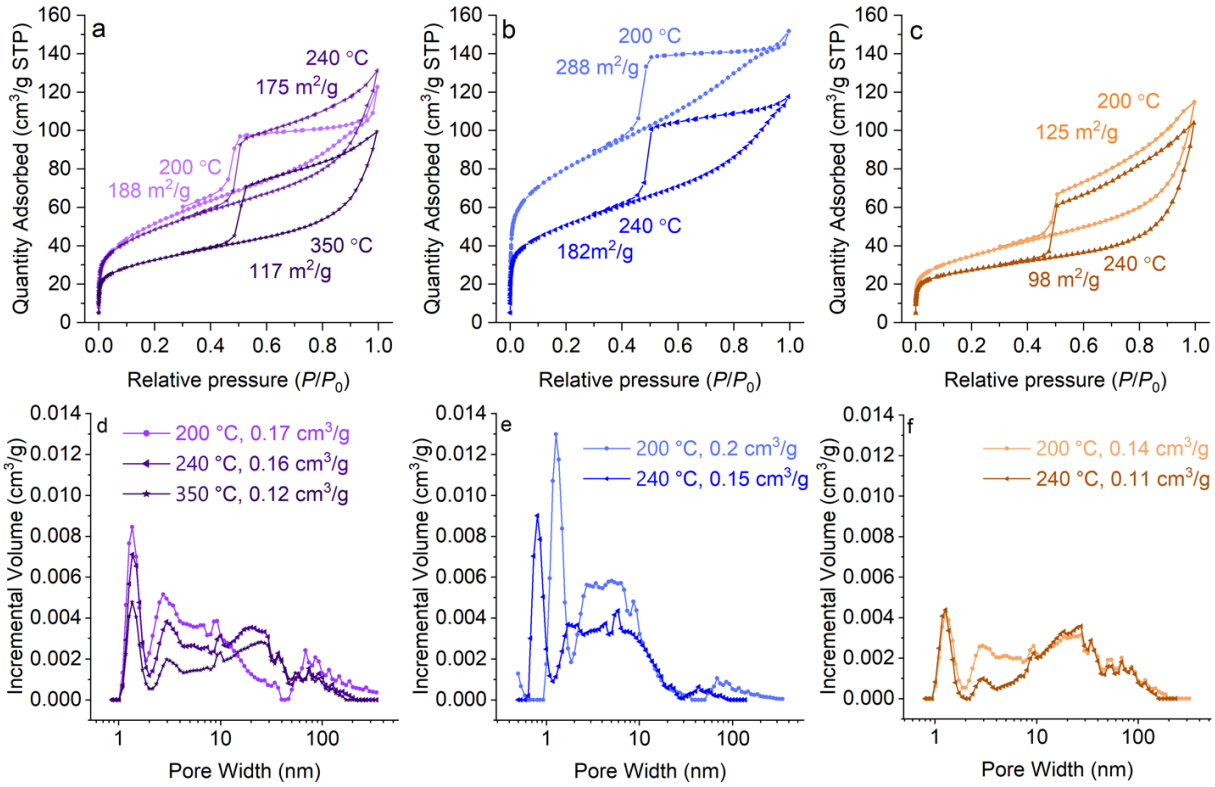

FIG. 2. Results of low-temperature nitrogen adsorption. N_2 adsorbtion/desorbtion isotherms for $x =$ a) 0.5, b) 0.7, and c) 1 together with BET surface area values. Pore size distribution and total pore volume for $x =$ d) 0.5, e) 0.7, and f) 1

atomic emission spectroscopy showed a ratio of Li:Mg = 1:3 – 1:2, which was expectedly underestimated due to the excess of positive charge of the phyllosilicate layer.

It should be noted that the Si/(Mg+Fe) ratio was closer to that of phyllosilicates with sepiolite and talc structures. However, based on the peak positions and intensity ratios, all PXRD patterns (Fig. 1a) corresponded precisely to phases with montmorillonite/saponite structures (including $x = 1$). This circumstance suggests that, to compensate for the lack of silicon, some of the Fe^{3+} cations may be incorporated into the tetrahedral position. According to Mössbauer spectroscopy data (Fig. 3a,b), two main (# 2 and # 3 in Fig. 3b) and one additional "doublet" (# 1) were detected for the products of hydrothermal treatment at 200 °C. Based on the combination of the isomer shift (IS) and quadrupole splitting (QS) values (Table A1), "doublet" # 1 was actually a part of sextet belonging to iron oxides. Based on the share of these minima in the total transmittance, it can be concluded that the content of oxide phase impurity remained negligibly small at $x > 0.6$, and a further abrupt increase in its content was associated with reaching the concentration limit of Fe^{3+} content in the phyllosilicate structure. In the products of phyllosilicate treatment at 200 °C, the presence of oxide was not detected at any x (Fig. 1a), probably due to the lower sensitivity of the method, as well as the X-ray wavelength and Fe absorption effect. The ratio of the two main doublets was on average 80:20 (Fig. 3b), regardless of the iron content. Similar distribution of Fe^{3+} between the octahedral and tetrahedral sites in layered silicates related in structure was noted in [47]. At the same time, the IS and QS values for the smaller doublet in our case were not entirely typical for iron cations in the tetra-position ($^{IV}Fe^{3+}$). If this doublet was erroneously attributed to $^{IV}Fe^{3+}$ instead of, for example, a variation in the octa-position ($^{VI}Fe^{3+}$) due to a change in the type of nearest neighbors, then a correlation between the doublet ratio and the iron content in the system would be expected, which, apparently, was not observed. The larger IS value compared to the data in [47] could be due to the increased unit cell parameters and the ^{IV}Me–O distance [48] in the hydrothermal treatment products compared to natural minerals. In addition, the presence of Li^+ instead of more widespread cations (Na^+, Ca^{2+}, and others) could make a significant contribution to the variation in both IS and QS values [49].

The effect of hydrothermal treatment temperature was considered for the case of the maximum iron content $x = 0.5$ (Fig. 3c). Increasing the treatment temperature to 240 °C resulted in the appearance of sextets in the Mössbauer spectra with parameters (Table A2) typical for spinel of variable composition $Mg_yFe_{2-y}O_4$, as well as α-Fe_2O_3. A further increase in the treatment temperature resulted in a quantitative, rather than qualitative, change in the nature of the iron distribution between the silicate and oxide phases. It is also worth noting the decrease in the line widths of the sextets with increasing hydrothermal treatment temperature, caused by an increase in the crystallinity of the phases.

TABLE 1. Element ratios estimated by the EDS method

Element	x in $Li_{2x}Fe_{2-2x}Mg_{2x}Si_4O_{10}(OH)_2$					
	0.5	0.6	0.7	0.8	0.9	1
calculated						
Fe	1	0.8	0.6	0.4	0.2	0
Mg	1	1.2	1.4	1.6	1.8	2
Si	4	4	4	4	4	4
200 °C hydrothermal treatment						
Fe	1.3	0.8	0.5	0.6	0.3	0.0
Mg	1.3	1.8	1.9	2.0	2.0	2.4
Si	4.0	4.0	4.0	4.0	4.0	4.0
Si/(Fe+Mg)	1.6	1.5	1.6	1.5	1.7	1.6
(Si+0.2Fe)/(0.8Fe+Mg)	1.9	1.7	1.8	1.6	1.8	1.6
240 °C hydrothermal treatment						
Fe	1.4	1.0	0.8	0.5	0.3	0.0
Mg	1.6	1.6	1.9	2.1	2.1	2.5
Si	4.0	4.0	4.0	4.0	4.0	4.0
Si/(Fe+Mg)	1.3	1.6	1.5	1.6	1.7	1.6
(Si+0.2Fe)/(0.8Fe+Mg)	1.6	1.8	1.7	1.7	1.7	1.6

If we take the average ratio of 80:20 for the distribution between $^{VI}Fe^{3+}$ and $^{IV}Fe^{3+}$ and introduce the appropriate correction for the EDS results (Table 1), the resulting ratio will approach that characteristic of phyllosilicates with MMT structure. The possibility of replacing a significant amount of Si^{4+} with Fe^{3+}, despite the large difference in effective ionic radii, was due to the layered crystal structure, which expands the limits of miscibility [50, 51]. In addition, the results of DFT calculations carried out earlier for the case of substitution of Mg^{2+} and Si^{4+} for 1:1 type chrysotile structure [52] revealed close energy equivalence of the substitution schemes exclusively in the octahedral sheet with formation of vacancy ($3Mg^{2+} = 2\,^{VI}Fe^{3+}$ + v) and simultaneous substitution in two sheets ($Mg^{2+} + Si^{4+} = {}^{VI}Fe^{3+} + {}^{IV}Fe^{3+}$).

Additional attempts to investigate the nature of iron distribution in the hydrothermal treatment products were made using diffuse reflectance spectroscopy. Fig. 4 shows recalculated absorption spectra of two spectral ranges obtained using the Kubelka–Munk function. For 200 °C hydrothermal treatment products, two broad absorption maxima appeared in the range of 300 – 400 nm at $x \leq 0.6$, corresponding to the formation of Fe-containing oxide nanoparticles [53]. In the range of 400 – 700 nm, changes in the absorption spectrum also occurred in the form of the appearance of two maxima in the region of 500 – 600 nm, characteristic for iron oxides [54, 55]. The changes in the optical spectra correlated with the results of Mössbauer spectra deconvolution, particularly with the increase in the content of #1 "doublet" (Fig. 3b). Based on the shape of the spectra, it can be concluded that with an increase in the hydrothermal treatment temperature to 240 °C, the formation of impurity phases began even at the minimum iron content in the system ($x = 0.9$). Thus, the synthesized Li–Fe-containing phyllosilicates with a montmorillonite structure exhibited a series of absorption peaks with maxima at 330, 510, and 630 nm.

An assessment of the band gap of the samples using optical spectroscopy showed that, regardless of the hydrothermal treatment temperature, the E_g value decreased almost linearly from 3.7 eV (at $x = 0.8$) to 3.1 eV (at $x = 0.5$). Given the obtained information on the phase composition, the observed value cannot be fully attributed to any one of the phases. At high iron content, E_g tended to the range of values characteristic of Fe_3O_4 [56], while from above it was limited by the capabilities of the spectrometer.

3.3. Temperature shift of silicate crystallization effect

Figure 5(a) shows the TG and DTG curves of 200 °C hydrothermal treatment products with different iron content. At the initial stage of heating, all samples exhibited significant mass loss due to the removal of adsorbed water. The magnitude of the loss correlated with the previously observed extreme dependence of the specific surface area on the

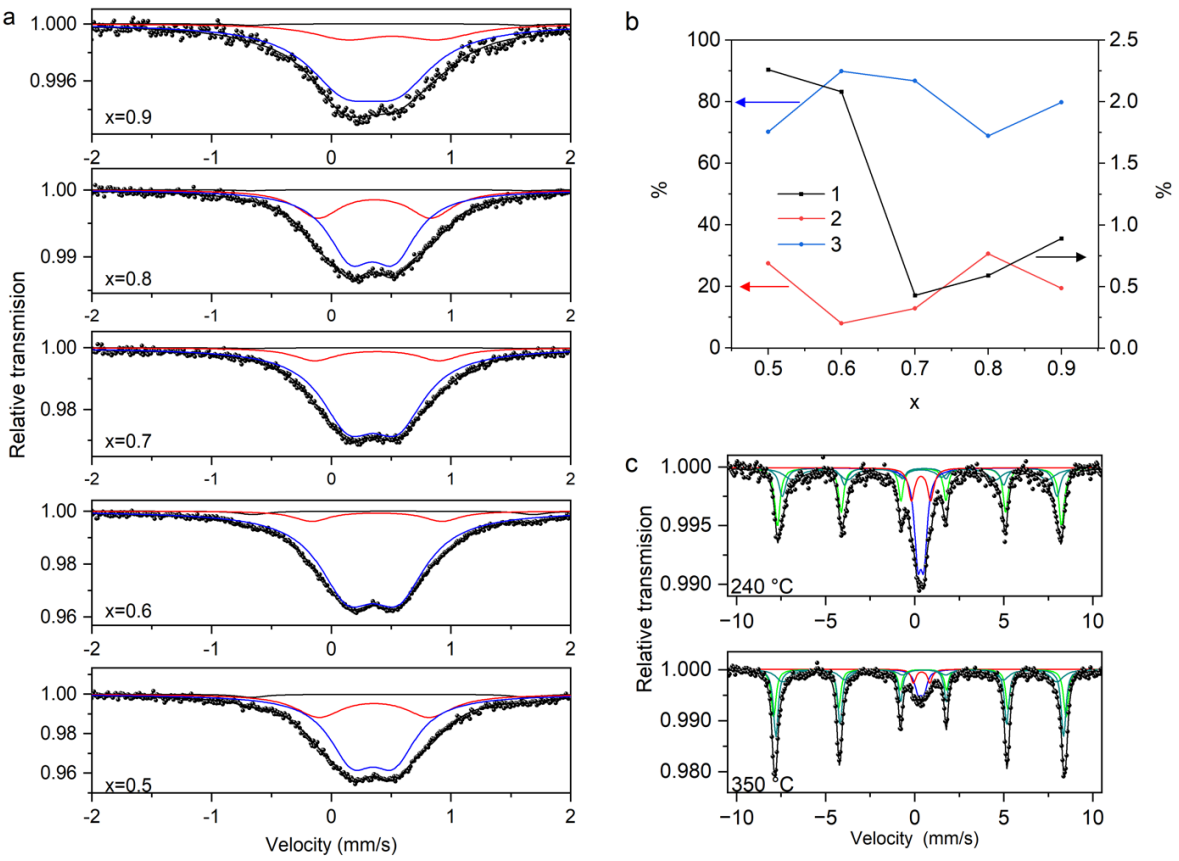

FIG. 3. Results of Mössbauer spectroscopy. a) Mössbauer spectra of 200 °C hydrothermal treatment products. b) Dependence of relative area of three doublets upon iron content. c) Mössbauer spectra of 240 and 350 °C hydrothermal treatment products with $x = 0.5$. Doublets and sextet parameters are shown in Tables A1, A2

iron content (Fig. 2): it was minimal at the edges of the studied x range and maximal at intermediate points. With further heating, the samples lost mass at virtually the same rate up to 450 °C, at which point a low-intensity loss peak was observed in the DTG curves of the samples with $x < 0.9$ (Fig. 5a). As a rule, the temperature range of 450 – 600 °C is characterized by mass losses caused by bulk dehydroxylation of phyllosilicates [57–59]. Compared to 1:1 type layered silicates, the studied 2:1 type silicate has two times less OH groups per formula unit, and therefore the effect was much weaker. Further, for most samples, a sharp peak in mass losses was observed with an intensity proportional to the magnesium content and probably caused by crystallization of (Mg,Fe)SiO_3 pyroxene and SiO_2 cristobalite (Fig. 6).

An interesting feature of the studied samples was the temperature dependence of the last mass loss peak (Fig. 5d,f). Thus, for the case of $x = 0.5$, the shift was about 75 °C with an increase in the hydrothermal treatment temperature from 200 to 240 °C (Fig. 5d). The phase composition of the samples after thermal analysis also varied (Fig. 6): for the sample obtained at 200 °C, the main part consisted of the phases (Mg,Fe)SiO_3, SiO_2, and traces of $Li_2Si_2O_5$, while for the products of hydrothermal treatment at higher temperatures, the main phase was $LiFeSi_2O_6$ with traces of (Mg,Fe)SiO_3 and SiO_2. Except for lithium silicate, all components are products of the decomposition reaction (for $x = 0.5$):

$$LiFeMgSi_4O_{10}(OH)_2 \rightarrow LiFeSi_2O_6 + MgSiO_3 + SiO_2 + H_2O \uparrow .$$

A probable reason for the differences in the observed phase composition after thermal analysis could be the difference in the content of the most mobile component – lithium. Under the conditions of low-temperature hydrothermal treatment (200 °C) and, as a result, small crystallite size (Fig. 1g), Li^+ could be easily washed out of the interlayer space during the process of purification from the solution that served as the hydrothermal environment. An increase in the treatment temperature led to a several-fold increase in the crystallite sizes, and consequently, the linear dimensions of the layers, which complicated the removal of lithium cations. In addition, an increase in temperature contributed to an increase in the entropy factor for the process of Li^+ incorporation directly into the phyllosilicate layer [32, 60].

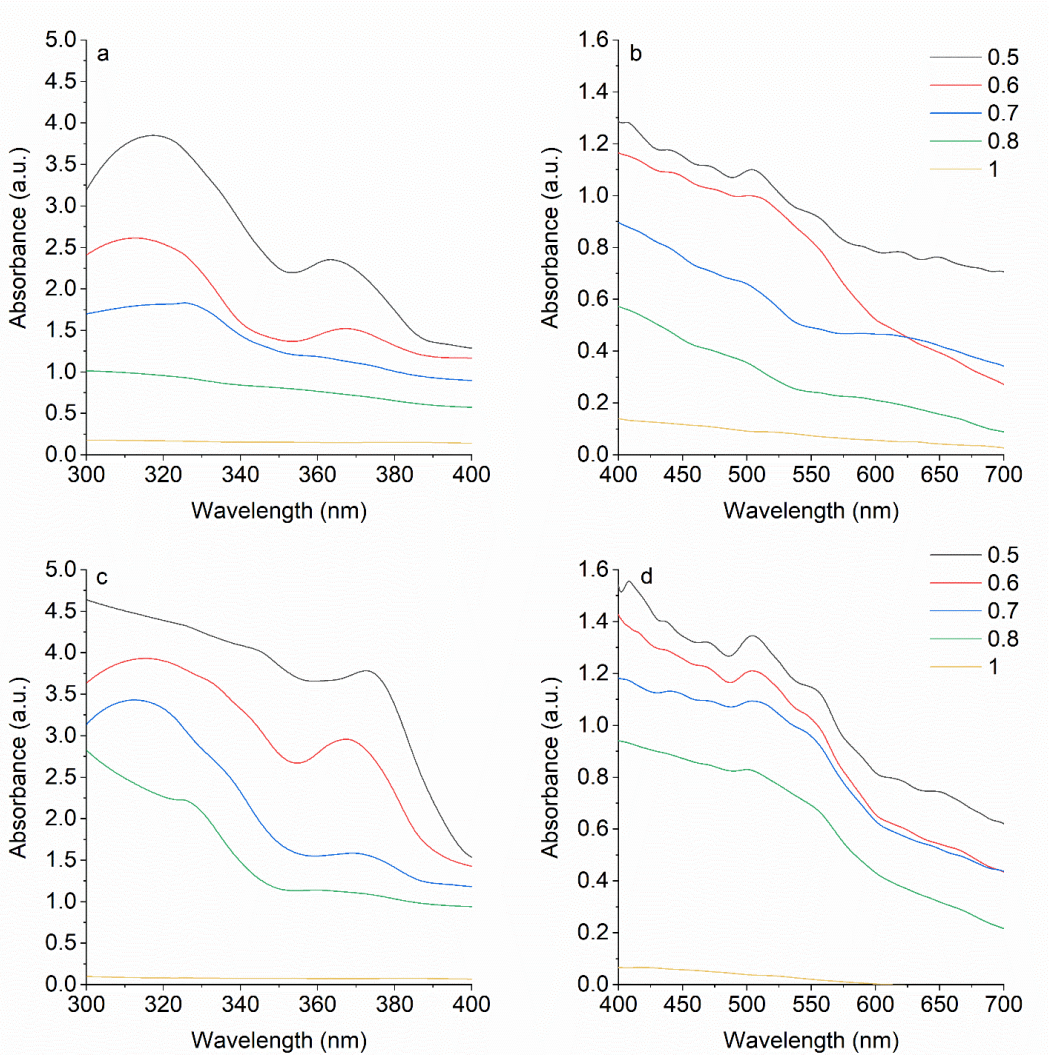

FIG. 4. UV-visible spectra recalculated from diffuse reflectance data for hydrothermal treatment products with $x = 0.5,\ 0.6,\ 0.7,\ 0.8$, and 1 obtained at a,b) 200 °C and c,d) 240 °C

4. Conclusion

The study demonstrated the feasibility of hydrothermal synthesis of Li–Fe phyllosilicates with a montmorillonite-like structure and a minimal amount of impurity phases in the form of Fe_3O_4 and Fe_2O_3-based solid solutions. Using a combination of diffraction and spectroscopic methods, the temperature and concentration thresholds for the formation of oxide phases were established. Thus, the formation of virtually single-phase products should be expected in the temperature range of 200 – 240 °C for x in the calculated chemical formula $Li_{2x}Fe_{2-2x}Mg_{2x}Si_4O_{10}(OH)_2$ being in the range of 0.8 – 1. The specific surface area was shown to depend on the iron content and reach a maximum in the range of $x = 0.7 - 0.8$. It was found that, due to the broader charge compensation capabilities of a multicomponent system, various deviations from the specified stoichiometry are possible within the layer, due to both the substitution of silicon cations by iron cations in the tetrahedral position (approximately 20 % of the total iron content) and the removal of some lithium cations from the interlayer space. Thermal analysis and X-ray diffraction revealed the role of MMT particle size factor and hydrothermal treatment temperature in the retention of lithium cations.

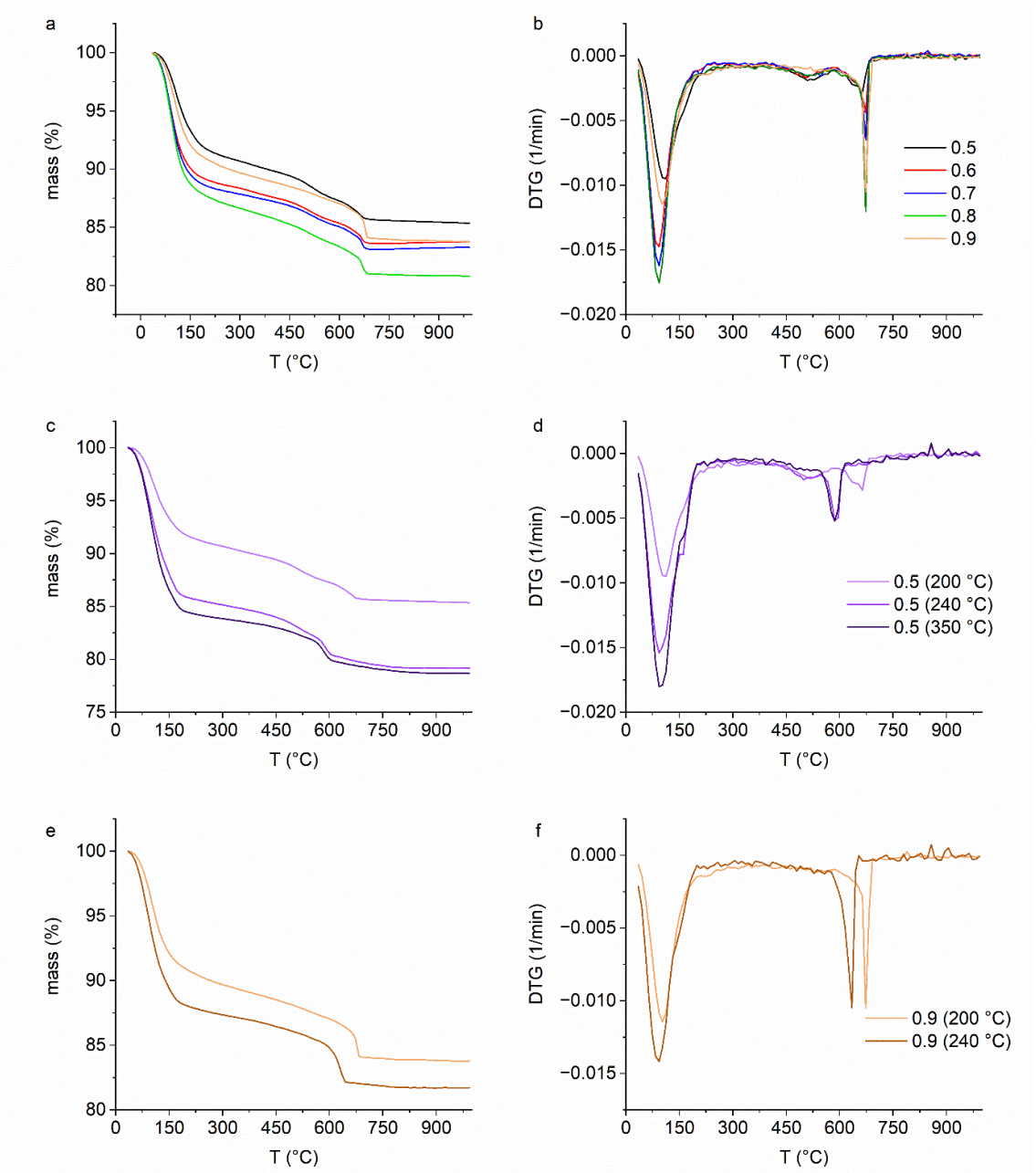

FIG. 5. TG and DTG curves of: a,b) 200 °C hydrothermal treatment products with different x; samples with $x =$ c,d) 0.5 and e,f) 0.9, obtained at various temperatures

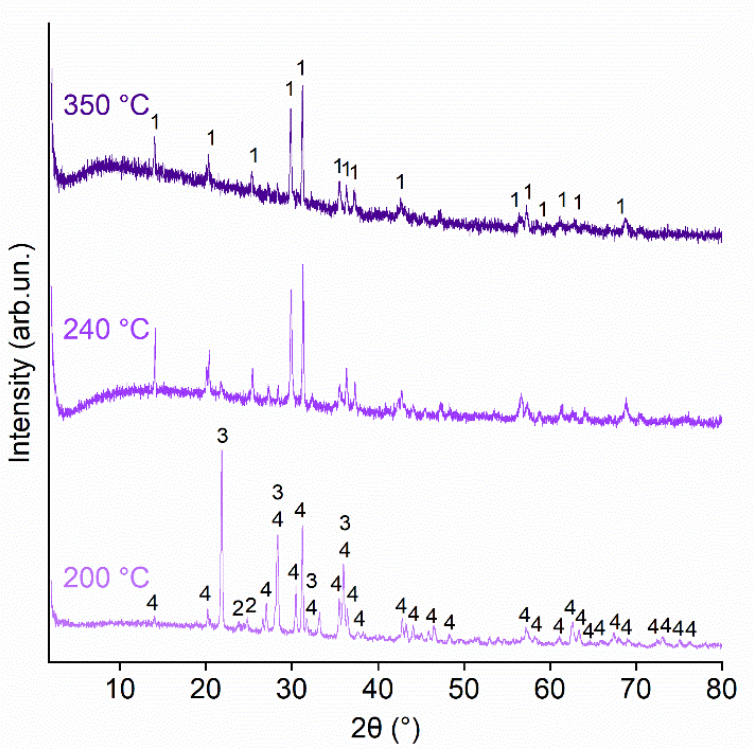

FIG. 6. Post-thermal analysis PXRD patterns of samples with $x = 0.5$ obtained at various hydrothermal treatment temperatures. Phase analysis was carried out using PDF-2 database: "1" – $LiFeSi_2O_6$ (89-225), "2" – $Li_2Si_2O_5$ (40-376), "3" – SiO_2 (75-923), "4" – $MgSiO_3$ (71-786)

Appendix

TABLE A1. Parameters of doublets observed by Mössbauer spectroscopy for 200 °C hydrothermal treatment products

x	Peak #	Width (mm/s)	IS (mm/s)	QS (mm/s)	%
0.5	1	0.278	0.48	2.32	2.2
	2	0.479	0.36	0.92	27.5
	3	0.466	0.35	−0.35	70.3
0.6	1	0.278	0.52	2.35	2.1
	2	0.366	0.38	1.09	8.0
	3	0.575	0.35	−0.43	89.9
0.7	1	0.278	0.48	2.30	0.4
	2	0.441	0.38	1.04	12.8
	3	0.561	0.35	−0.41	86.8
0.8	1	0.278	0.48	2.31	0.6
	2	0.448	0.36	0.94	30.6
	3	0.466	0.34	−0.37	68.8
0.9	1	0.278	0.48	2.30	0.9
	2	0.691	0.51	0.76	19.4
	3	0.736	0.33	−0.45	79.8

TABLE A2. Peak parameters observed by Mössbauer spectroscopy for 240 and 350 °C hydrothermal treatment products with $x = 0.5$

T (°C)	Peak #	Width (mm/s)	IS (mm/s)	QS (mm/s)	Heff (mm/s)	%
240	Doublets					
	2	0.420	0.36	1.08	–	8.8
	3	0.440	0.34	0.34	–	23.7
	Sextets					
	Fe_2O_3	0.363	0.38	0.22	49.5	30.9
		0.340				
		0.315				
	Fe_3O_4 (A)	0.464	0.40	0.25	47.9	16.8
		0.444				
		0.423				
	Fe_3O_4 (B)	1.128	0.33	0.10	44.5	19.8
		0.932				
		0.757				
350	Doublets					
	2	0.308	0.39	0.92	–	3.6
	3	0.443	0.35	0.32	–	7.8
	Sextets					
	Fe_2O_3	0.316	0.38	0.19	51.0	28.6
		0.293				
		0.284				
	Fe_3O_4 (A)	0.314	0.38	0.21	50.1	40.7
		0.298				
		0.282				
	Fe_3O_4 (B)	0.875	0.41	0.23	47.8	19.3
		0.759				
		0.671				

References

[1] Perim E., Machado L.D., Galvao D.S. A brief review on syntheses, structures, and applications of nanoscrolls. *Front. Mater.*, 2014, **1** (2003), P. 1–17.

[2] Krasilin A.A., Khrapova E.K., Maslennikova T.P. Cation Doping Approach for Nanotubular Hydrosilicates Curvature Control and Related Applications. *Crystals*, 2020, **10** (8), 654.

[3] Gatina E.N., Maslennikova T.P. Formation of chrysotile nanotubes with titania in the internal channel. *Nanosystems: Physics, Chemistry, Mathematics*, 2024, **15** (3), P. 380–387.

[4] Kurguzkina M.E., Maslennikova T.P., Gusarov V.V. Formation, Morphology, and Size Parameters of Nanopowders Based on $Mg_3Si_2O_5(OH)_4$–$Ni_3Si_2O_5(OH)_4$ Nanoscrolls. *Inorganic Materials*, 2023, **59** (10), P. 1075–1084.

[5] Drits V.A., Besson G., Muller F. An Improved Model for Structural Transformations of Heat-Treated Aluminous Dioctahedral 2:1 Layer Silicates. *Clays Clay Miner.*, 1995, **43** (6), P. 718–731.

[6] Emmerich K., et al. Clay profiling: The classification of montmorillonites. *Clays Clay Miner.*, 2009, **57** (1), P. 104–114.

[7] García-Romero E., et al. On the structural formula of smectites: a review and new data on the influence of exchangeable cations. *J. Appl. Crystallogr.*, 2021, **54** (1), P. 251–262.

[8] Zango Z.U., et al. Montmorillonite for Adsorption and Catalytic Elimination of Pollutants from Wastewater: A State-of-the-Arts Review. *Sustainability*, 2022, **14** (24), 16441.

[9] França D.B., et al. The versatility of montmorillonite in water remediation using adsorption: Current studies and challenges in drug removal. *J. Environ. Chem. Eng.*, 2022, **10** (2), 107341.

[10] Kryuchkova M., et al. Pharmaceuticals Removal by Adsorption with Montmorillonite Nanoclay. *Int. J. Mol. Sci.*, 2021, **22** (18), 9670.

[11] Golubeva O.Yu., et al. Increased Adsorption of Ciprofloxacin by Systematic Variation of the Composition of Synthetic Montmorilloinites. *ACS Appl. Nano Mater.*, 2025, **8** (16), P. 8489–8498.

[12] Polotskaya G.A., et al. Structure and Transport Properties of Cellulose Acetate/Montmorillonite Composites. *Membranes and Membrane Technologies*, 2022, **4** (6), P. 367–376.

[13] Dumitru M.V., et al. Organically modified montmorillonite as pH versatile carriers for delivery of 5-aminosalicylic acid. *Appl. Clay Sci.*, 2022, **218**, 106415.

[14] Nuruzzaman M., et al. Capability of Organically Modified Montmorillonite Nanoclay as a Carrier for Imidacloprid Delivery. *ACS Agricultural Science & Technology*, 2022, **2** (1), P. 57–68.

[15] Ovchinnikov N.L., et al. The Preparation of Self-Cleaning Wool-Fiber–TiO_2-Pillared Montmorillonite Composites with UV-Protection Properties. *Protection of Metals and Physical Chemistry of Surfaces*, 2023, **59** (3), P. 377–383.

[16] Karthikeyan K., Thirumoorthi A. $BiFeO_3$-Montmorillonite intercalated nano composites – synthesis and its characterization. *Nanosystems: Physics, Chemistry, Mathematics*, 2018, P. 631–640.

[17] Huang W.J., et al. Recent advances in engineering montmorillonite into catalysts and related catalysis. *Catal. Rev. Sci. Eng.*, 2023, **65** (3), P. 929–985.

[18] Wu L., et al. Montmorillonite-based materials for electrochemical energy storage. *Green Chemistry*, 2024, **26** (2), P. 678–704.

[19] Chen C., Ma Y., Wang C. Investigation of electrochemical performance of montmorillonite clay as Li-ion battery electrode. *Sustainable Materials and Technologies*, 2019, **19**, e00086.

[20] Hao L., et al. Interlayer cation effects on optical and dielectric properties of montmorillonite in terahertz frequency band. *Appl. Clay Sci.*, 2025, **274**, 107857.

[21] Qin Y., et al. Effect of Montmorillonite Layer Charge on the Thermal Stability of Bentonite. *Clays Clay Miner.*, 2021, **69** (3), P. 328–338.

[22] Berdinazarov Q., Khakberdiev E., Ashurov N. The effect of layered silicates on the morphological, rheological and mechanical properties of PA and PP blends. *Nanosystems: Physics, Chemistry, Mathematics*, 2024, **15** (3), P. 410–417.

[23] Makarov V.N., Kanygina O.N. Model of destruction of montmorillonite crystal structure in a microwave field. *Nanosystems: Physics, Chemistry, Mathematics*, 2020, **11** (2), P. 153–160.

[24] Zhang Y., et al. Separators Modified with Ultrathin Montmorillonite/Polymer Nanocoatings Achieve Dendrite-Free Lithium Deposition at High Current Densities. *Nano Lett.*, 2024, **24** (29), P. 8834–8842.

[25] Gorospe A.E.G., et al. Ultralong cycle lifespan in lithium metal batteries Unlocked by a lithiophilic montmorillonite separator. *Mater. Lett.*, 2025, **401**, 139240.

[26] Para M.L., et al. Synthesis and characterization of montmorillonite/polyaniline composites and its usage to modify a commercial separator. *Journal of Electroanalytical Chemistry*, 2021, **880**, 114876.

[27] Wang W., Yang Y., Zhang J. Boosting Li^+ Conductivity and Oxidation Stability of Solid Polymer Electrolytes Using a Sustainable Montmorillonite-Based Ion Conductor. *Nano Lett.*, 2025, **25** (10), P. 3867–3874.

[28] Zhou S., et al. Low-cost and high-safety montmorillonite-based solid electrolyte for lithium metal batteries. *Appl. Clay Sci.*, 2024, **251**, 107329.

[29] Wang L., et al. Bifunctional lithium-montmorillonite enabling solid electrolyte with superhigh ionic conductivity for high-performanced lithium metal batteries. *Energy Storage Mater.*, 2023, **63**, 102961.

[30] Yan H., Zhang Z. Effect and mechanism of cation species on the gel properties of montmorillonite. *Colloids and Surfaces A: Physicochemical and Engineering Aspects*, 2021, **611**, 125824.

[31] Wu Z., et al. Thermal Migration Behavior of Na^+, Cu^{2+} and Li^+ in Montmorillonite. *Minerals*, 2022, **12** (4), 477.

[32] Wu Z., et al. The migration and occupation of Li^+ and Na^+ in illite and montmorillonite during the heating process. *Mineral Mag.*, 2024, **88** (5), P. 536–545.

[33] Semenov V.G., Moskvin L.N., Efimov A.A. Analytical potential of Mössbauer spectroscopy. *Russian Chemical Reviews*, 2006, **75** (4), P. 317–327.

[34] Grażulis S., et al. Crystallography Open Database (COD): an open-access collection of crystal structures and platform for world-wide collaboration. *Nucleic Acids Res.*, 2012, **40** (D1), P. D420–D427.

[35] Brunauer S., Emmett P.H., Teller E. Adsorption of Gases in Multimolecular Layers. *JACS*, 1938, **60** (2), P. 309–319.

[36] Sing K.S.W. Reporting physisorption data for gas/solid systems with special reference to the determination of surface area and porosity (Recommendations 1984). *Pure and Applied Chemistry*, 1985, **57** (4), P. 603–619.

[37] Klein J., et al. Limitations of the Tauc Plot Method. *Adv. Funct. Mater.*, 2023, **33** (47).

[38] Gournis D., et al. A neutron diffraction study of alkali cation migration in montmorillonites. *Phys Chem Miner.*, 2008, **35** (1), P. 49–58.

[39] Antao S.M., Hassan I., Parise J.B. Cation ordering in magnesioferrite, $MgFe_2O_4$, to 982 °C using in situ synchrotron X-ray powder diffraction. *American Mineralogist*, 2005, **90** (1), P. 219–228.

[40] Maslen E.N., et al. Synchrotron X-ray study of the electron density in α-Fe_2O_3. *Acta Crystallogr. B*, 1994, **50** (4), P. 435–441.

[41] Korytkova E.N., et al. Hydrothermal synthesis of nanotubular Mg-Fe hydrosilicate. *Russian J. of Inorganic Chemistry*, 2007, **52** (3), P. 338–344.
[42] Krasilin A.A., et al. Formation of variable-composition iron(III) hydrosilicates with the çhrysotile structure. *Russ. J. Gen. Chem.*, 2016, **86** (12), P. 2581–2588.
[43] Bloise A., et al. Synthesis of Fe-doped chrysotile and characterization of the resulting chrysotile fibers. *Crystal Research and Technology*, 2009, **44** (6), P. 590–596.
[44] Shannon R.D., Prewitt C.T. Effective ionic radii in oxides and fluorides. *Acta Crystallogr B.*, 1969, **25** (5), P. 925–946.
[45] Khramchenkov M.G., et al. Microstructural transformations of swelling clay minerals. *Georesursy*, 2023, **25** (1), P. 108–118.
[46] Khrapova E.K., Kozlov D.A., Krasilin A.A. Hydrothermal Synthesis of Hydrosilicate Nanoscrolls $(Mg_{1-x}Co_x)_3Si_2O_5(OH)_4$ in a Na_2SO_3 Solution. *Russian J. of Inorganic Chemistry*, 2022, **67** (6), P. 839–849.
[47] Cuadros J., et al. Controls on tetrahedral Fe(III) abundance in 2:1 phyllosilicates. *American Mineralogist*, 2019, **104** (11), P. 1608–1619.
[48] Annersten H., Olesch M. Distribution of ferrous and ferric iron in clintonite and the Mössbauer characteristics of ferric iron in tetrahedral coordination. *Can. Mineral.*, 1978, **16**, P. 199–203.
[49] Darby Dyar M. A review of Mössbauer data on trioctahedral micas: Evidence for tetrahedral Fe^{3+} and cation ordering. *American Mineralogist*, 1987, **72**, P. 102–112.
[50] Almjasheva O.V., et al. Structural features of ZrO_2-Y_2O_3 and ZrO_2-Gd_2O_3 nanoparticles formed under hydrothermal conditions. *Russ. J. Gen. Chem.*, 2014, **84** (5), P. 804–809.
[51] Almjasheva O.V., Krasilin A.A., Gusarov V.V. Formation mechanism of core-shell nanocrystals obtained via dehydration of coprecipitated hydroxides at hydrothermal conditions. *Nanosystems: Physics, Chemistry, Mathematics*, 2018, **9** (4), P. 568–572.
[52] Krasilin A.A., et al. Young's and shear moduli of Fe^{3+}- doped chrysotile nanoscrolls probed by atomic force microscopy. *Mater. Today Commun.*, 2024, **38**, 108358.
[53] Borghi E., et al. Spectroscopic characterization of Fe-doped synthetic chrysotile by EPR, DRS and magnetic susceptibility measurements. *Phys. Chem. Chem. Phys.*, 2010, **12** (1), P. 227–238.
[54] Kulkarni S.A., et al. Effect of synthesis route on the structural, optical and magnetic properties of Fe_3O_4 nanoparticles. *Ceram. Int.*, 2014, **40** (1), P. 1945–1949.
[55] Mitra S., et al. Synthesis of a α-Fe_2O_3 nanocrystal in its different morphological attributes: growth mechanism, optical and magnetic properties. *Nanotechnology*, 2007, **18** (27), 275608.
[56] Kouotou P.M., et al. Particle size-band gap energy-catalytic properties relationship of PSE-CVD-derived Fe_3O_4 thin films. *J. Taiwan Inst. Chem. Eng.*, 2018, **93**, P. 427–435.
[57] Trittschack R., Grobéty B., Brodard P. Kinetics of the chrysotile and brucite dehydroxylation reaction: a combined non-isothermal/isothermal thermogravimetric analysis and high-temperature X-ray powder diffraction study. *Phys. Chem. Miner.*, 2014, **41** (3), P. 197–214.
[58] Qin M., et al. In-situ observation of nanoscale transformations in dehydrating lizardite. *Sci Rep.*, 2025, **15** (1), 4000.
[59] Khrapova E.K., et al. Thermal behavior of Mg-Ni-phyllosilicate nanoscrolls and performance of the resulting composites in hexene-1 and acetone hydrogenation. *ChemNanoMat.*, 2021, **7** (3), P. 257–269.
[60] Li Q., et al. Revealing atomistic mechanism of lithium diffusion in montmorillonite structure: A molecular simulation study. *Geochim. Cosmochim. Acta*, 2025, **392**, P. 165–174.

Submitted 14 November 2025; accepted 2 December 2025

Information about the authors:

Asiyat A. Iyakhmaeva – Ioffe Institute, 194021 St. Petersburg, Russia; acya.gitinova@gmail.com

Ekaterina K. Khrapova – Ioffe Institute, 194021 St. Petersburg, Russia; ORCID 0000-0003-2674-9653; e.k.khrapova@mail.ioffe.ru

Lev A. Lebedev – Ioffe Institute, 194021 St. Petersburg, Russia; ORCID 0000-0001-9449-9487; L.A.Lebedev@mail.ioffe.ru

Nadezhda V. Glebova – Ioffe Institute, 194021 St. Petersburg, Russia; ORCID 0000-0003-4519-0111; Glebova@mail.ioffe.ru

Valentin G. Semenov – Institute of Chemistry, Saint Petersburg State University, 199034 St. Petersburg, Russia; ORCID 0000-0002-1530-7289; val_sem@mail.ru

Andrey V. Kopylov – RITVERC JSC, St. Petersburg, 194223, Russia; akopylov@ritverc.com

Andrei A. Krasilin – Ioffe Institute, 194021 St. Petersburg, Russia; ORCID 0000-0002-3938-3024; ikrasilin@mail.ioffe.ru

Conflict of interest: the authors declare no conflict of interest.